A phase field model for dislocations in hexagonal close packed crystals

C. Albrecht [a,*], A. Hunter [b], A. Kumar [c], I.J. Beyerlein [a,d]

[a] *Materials Department, University of California, Santa Barbara Santa Barbara, CA 93106, USA*
[b] *X Computational Physics Division, Los Alamos National Laboratory Los Alamos, NM 87545, USA*
[c] *Theoretical Division, Los Alamos National Laboratory Los Alamos, NM, 87545, USA*
[d] *Department of Mechanical Engineering, University of California, Santa Barbara Santa Barbara, CA 93106, USA*

ARTICLE INFO

ABSTRACT

In this work, an application of a phase field formulation suitable for modeling the motion of individual partial and full dislocations in hexagonal close packed (HCP) crystals is presented. The formulation incorporates periodic potentials for glide on the distinct HCP slip systems, which are informed here by density functional theory (DFT). The model is applied to simulate the dissociation process starting from an unstable perfect dislocation and ending at its final equilibrium structure for different slip planes and in different HCP metals. The structural characteristics that are predicted for these dislocations include the partial Burgers vectors, dissociation distances, core widths of the partials, and any asymmetries in these quantities. Mg is selected as one of the model materials since its dislocations are the most well studied and it is nearly elastically isotropic. For Mg, it is shown that the predictions for dissociation distances agree with those reported previously by atomic-scale calculations, including density functional theory, for dislocations on the basal $<a>$, prismatic $<a>$, and pyramidal type II $<c+a>$ slip systems. Phase field model results are also presented for dislocations in Ti and Zr, which we find develop distinctively different equilibrium structures than Mg.

© 2019 Published by Elsevier Ltd.

1. Introduction

The plastic deformation response of materials with a hexagonal close packed (HCP) crystal structure is governed by the glide of dislocations on both low index and high index planes (Partridge, 1967). Each mode of slip is defined by the specific slip plane and slip direction of these dislocations (Partridge, 1967; Yoo, 1969). For an HCP crystal, whether it deforms in a brittle or ductile manner depends on the relative amounts of moving dislocations contributed by each mode (Bertin et al., 2014). The ease of dislocation motion is largely a consequence of the characteristics of the dislocation core structure, such as number of planes on which is extends, whether it dissociates into smaller partial dislocations, its splitting distance, and the width of the individual partials.

For HCP crystals, the structure of the dislocation core depends on the type of glide plane and Burgers vector, the elastic strain, and the strain energy that the dislocation core generates in the surrounding material outside the core region. Most dislocation cores can be described as being dissociated into partial dislocations with a smaller Burgers vector and a stacking

---

* Corresponding author.
  E-mail address: claire_weaver@ucsb.edu (C. Albrecht).

fault in between (Kumar et al., 2017; Partridge, 1967; Wu et al., 2015; Yin et al., 2017). The spreading distance between the partials is governed primarily by the balance between the interaction strain energy between the partials and the energy required to form or grow the stacking fault (Hirth and Lothe, 1968). For the HCP Mg crystal, recent density functional theory (DFT) and Molecular Dynamics (MD) studies have calculated the core structures of dislocations of edge and screw character belonging to the basal $<a>$, prismatic $<a>$, and pyramidal $<c+a>$ modes (Kumar et al., 2017; Shen et al., 2014; Wu et al., 2015; Yasi et al., 2009). They are all shown to be planar, with the partials and associated core displacements predominantly acting in the slip plane. The basal $<a>$ dislocation dissociates into two partials with an intrinsic stacking fault in between, the prismatic $<a>$ dislocation remains compact, i.e., undissociated, and the pyramidal $<c+a>$ dislocation splits into two partials of equal Burgers vector separated by a stacking fault. For other structurally relevant metals, such as HCP Ti and Zr, far fewer DFT and MD studies on core structures currently exist (Clouet, 2012; Clouet et al., 2015; Domain and Besson, 2004; Udagawa et al., 2010).

Apart from core structures, atomistic simulations have been successful in modeling the motion of individual HCP dislocations (Wang et al., 2012; 2014a). Due to size limitations, the dynamics of dislocations have not been simulated by DFT. MD, given an interatomic potential, has been used to study the motion of a wide range of HCP crystals, such as Mg and Mg alloys, Zr, and Ti (Clouet, 2012; Shen et al., 2014; Wang and Beyerlein, 2012b; Wang et al., 2014a; Wu et al., 2015; Yin et al., 2017). Yet still, it is widely recognized that length and time scale limitations prevent the study of traditional size crystals ($>$ microns) and typical laboratory test conditions ($> 10^{-3}$/s). These limitations also make it prohibitive to model collections of dislocations.

As an alternative to atomic-scale simulations are continuum mechanics models that attempt to model directly an individual dislocation or dislocations moving on specific planes. These models are often referred to as mesoscale models, due to the length and/or time scales of the phenomenon they model as opposed to the theory or formulation on which they are based. The discrete dislocation dynamics (DDD) technique is one such example and has, for several decades, proven to be a powerful and effective tool for modeling from a few to several hundreds of individual dislocations, propagating within a number of crystal structures, including HCP crystals (Bertin et al., 2014; Capolungo et al., 2010). However, in DDD, dislocations are modeled as linear objects and the structure of the dislocation core is not resolved. Another class of continuum models are Peierls-Nabarro (P-N) models, or more recently generalized PN models (GPN), that calculate core structures of dislocations based on minimizing the elastic strain and lattice energies. But to date, these have been applied mostly to face-centered cubic (FCC) and body-centered cubic (BCC) crystals, with exception of (Wang et al., 2010), which investigated dislocations lying in the basal plane in Mg.

A third type of continuum mechanics models are those that adopt the framework of phase field (PF) theory and apply it to simulate the motion of discrete dislocations in single and polycrystalline systems (Beyerlein and Hunter, 2016; Cao et al., 2015; Hunter et al., 2018; Wang and Li, 2010). Traditionally, PF theory has been used to predict the temporal and spatial evolution of domain structures, whose distinguishing property is indicated by a set of order parameters, ζ (e.g., representing solute concentration, atomic order, polarization, dislocation slip) (Beyerlein and Hunter, 2016; Steinbach, 2009; Svendsen et al., 2018; Wang and Li, 2010). In PF-based discrete dislocation modeling, the general free energy density E of Cahn and Hilliard (1958) is made to depend on the total strain energy and stacking fault energy (SFE). The phase field order parameter, ζ_α, corresponds to the crystallographic shift caused by a gliding dislocation on the slip plane α. A coupled set of time-dependent Ginzburg-Landau equations is then employed to solve for ζ_α, at every time step. Accordingly, with this methodology, the values of ζ_α correspond to non-negative dissipation and gradient flow toward thermodynamic equilibrium. Like DDD and P-N/GPN models, PF dislocation mechanics models have primarily been employed to study dislocations in FCC crystals. Recent application of the PF approach to dislocation processes has seen treatment of the nucleation and motion of defects, such as dislocations and twins, and their interactions with surfaces, boundaries, and interfaces in FCC single crystals and polycrystalline materials (Beyerlein and Hunter, 2016; Hunter and Beyerlein, 2015; Hunter et al., 2018; Lei et al., 2013; Zeng et al., 2016). Only recently has PFDD been applied to BCC crystals, to study misfit dislocations in a BCC twist boundary or anisotropy in loop expansion under stress (Peng et al., 2019; Qiu et al., 2019). For glide processes relevant to HCP stacking, a few notable exceptions are the work by Louchez et al. (2017), who investigated the transition of the FCC to HCP structure via the glide of FCC Shockley partial dislocations, and by Zhao et al. (2019), who recently modeled slip transmission of Shockley partial dislocations on the basal plane in a Ti alloy across an HCP/BCC interface.

In this work, we build upon the 3D phase field dislocation formulation, called phase field dislocation dynamics (PFDD), presented in (Hunter and Beyerlein, 2013; 2014; 2015; Peng et al., 2019) and adapt it to treat dislocations on slip systems belonging to distinct slip modes in an HCP crystal. To demonstrate the method, we carry out calculations for a small selection of materials, Mg, as well as an MgY alloy, Ti and Zr that would be potentially distinct in the structures of their dislocation cores. The choice of Mg is particularly important since dislocations in Mg have been heavily studied by a number of other computational methods. It is nearly elastically isotropic and the dislocations belonging to the different slip modes are sufficiently distinct. The PFDD model requires as input the stacking fault energies on the different slip planes of HCP crystals, and here, the slip-plane energetic landscapes, called the generalized stacking fault energies, are calculated using DFT for Mg, Ti, and Zr. Use of DFT advantageously circumvents the need for reliable interatomic potentials from atomic-scale simulation. The extended HCP phase field dislocation model is applied to calculate the core structures of dislocations on the three common HCP slip modes: basal, prismatic, and pyramidal-type II. We compare these results with similar calculations by MD and DFT available in the literature to verify the model extensions. This 3D phase field method will be suitable for calculating the formation, motion and interaction of extended defects in strained HCP crystals.

2. Methodology

The PFDD formulation is general and application to different material systems falls largely on choice of energetic terms, and their parameters and functional forms. Up to now research has focused on cubic systems, and the energetic terms in the master energy functional have been selected to apply best to cubic crystal structures. Due to the symmetry of cubic materials, some simplifying assumptions could be made and here for the low symmetry of HCP crystals, these need to be re-evaluated. In this section we briefly review the PFDD approach and in the next section, we detail the energetic terms applicable for dislocations in HCP crystals.

2.1. The phase field approach for dislocations

Phase field formulations treat a 3D discretized system where every point is a thermodynamic system, whose free energy is specified as a function of the field variables of interest. A scheme is used to minimize the total system energy and solve for the corresponding values for the field variables. The field variables, or order parameters, are scalar-valued and evolve within the system. In the case of dislocations, the order parameters, ζ_α, represent the location of slip by dislocations in the slip system α. A physically based definition for these order parameters associates one order parameter with slip made by each slip system. In the case of an FCC crystal, there are 12 order parameters needed to fully describe dislocation dynamics in an FCC crystal (Beyerlein and Hunter, 2016; Koslowski et al., 2002; Wang et al., 2001). A mathematically based definition, however, considers a reduced set of order parameters associated with slip made by independent directions. For an FCC crystal, using this definition produces eight order parameters, consisting of a set of slip by both perfect and partial slip systems (Mianroodi and Svendsen, 2015).

In the dislocation problems of interest, the total free energy of the system consists of three contributions (Beyerlein and Hunter, 2016; Koslowski et al., 2002; Wang et al., 2001):

$$E = E^{strain} + E^{ext} + E^{lattice} \tag{1}$$

where E^{strain} is the elastic strain energy generated by a dislocation and dislocation-dislocation interactions, E^{ext} is work done to the system through an applied stress, and $E^{lattice}$ describes the energy expended as a dislocation glides through the crystal lattice breaking and re-forming atomic bonds. Some, but not all, phase field dislocation formulations (Mianroodi and Svendsen, 2015; Wang et al., 2001) include an energy term associated with the gradient in the order parameter. It is particularly relevant at the dislocation line, at the boundary between the slipped and unslipped region and its functional form depends on the configuration of the core, e.g., whether it is planar or non-planar, spread or compact. It is best informed by atomic-scale calculations, and in practice the term has introduced fitting parameter(s) to be adjusted according to an atomic scale core calculation. The impact of the additional gradient energy term has been reported in a few studies, each having focused on its effects for a particular FCC metal (Mianroodi et al., 2016; Pi et al., 2017; Shen and Wang, 2004; Xu et al., 2019). In this work, we elect to make independent comparisons between our dislocation structure calculations and those from other methods and to not add fit parameters. Therefore, in this first presentation of the HCP formulation, we neglect the gradient energy term, bearing in mind that it would straightforward to include it in later treatments.

Traditionally, the strain energy E^{strain} can be expressed as

$$E^{strain} = \frac{1}{2} \int C_{ijkl} \epsilon_{ij}^e(\mathbf{x}, t) \epsilon_{kl}^e(\mathbf{x}, t) d^3 x \tag{2}$$

where C_{ijkl} is the elastic moduli tensor. Through transformation into Fourier space, the elastic strain, ϵ^e, can be expressed in terms of the plastic strain, ϵ^p. The strain energy can then be written as

$$E^{strain} = \frac{1}{(2\pi)^3} \fint \frac{1}{2} \hat{A}_{mnuv}(\mathbf{k}) \hat{\epsilon}_{mn}^p(\mathbf{k}) \hat{\epsilon}_{uv}^{p*}(\mathbf{k}) d^3 k \tag{3}$$

where a superposed $\hat{()}$ denotes the Fourier transform, $\hat{A}_{mnuv}(\mathbf{k}) = C_{mnuv} - C_{kluv} C_{ijmn} \hat{G}_k(\mathbf{k}) k_j k_l$, $\mathbf{k}$ is the wavenumber vector, $\hat{G}_k(\mathbf{k})$ is the Fourier transform of the Green's tensor of linear elasticity, $\fint$ denotes the principal value of the integral, and the superscript $(*)$ denotes the complex conjugation.

The plastic strain ϵ^p results from the motion of dislocations and, therefore, can be expressed as a function of the order parameters (Koslowski et al., 2002; Wang et al., 2001):

$$\epsilon_{ij}^p = \frac{1}{2} \sum_{\alpha=1}^N b \zeta_\alpha(\mathbf{x}, t) \delta_\alpha (s_i^\alpha m_j^\alpha + s_j^\alpha m_i^\alpha). \tag{4}$$

The sum is taken over all slip systems from 1 to N included in the material, b is the magnitude of the Burgers vector, $\mathbf{m}$ is the slip plane normal, $\mathbf{s}$ is the slip direction (normalized Burgers vector), and δ_α is a Dirac distribution supported on the active slip planes. Considering again, as an example, the FCC crystal structure, wherein there are 12 slip systems belonging to the $\{111\} < 110 >$ slip mode and hence 12 order parameters. Dislocations on these systems are referred to as perfect dislocations since their Burgers vector corresponds to a lattice translation vector. The slip plane normals are of the $\{111\}$ type, slip directions are of the $< 110 >$ type, and $N = 12$ for all possible glide systems.

The external energy is given by:

$$E^{ext} = \int \sigma_{ij}^{appl} \epsilon_{ij}^p d^3x \tag{5}$$

where σ^{appl} is the applied stress tensor. Similar to the strain energy, the dependence on the order parameters comes through the expression of the plastic strain shown in Eq. (4).

The lattice energy $E^{lattice}$ represents the expenditure of breaking and reforming interlayer atomic bonds as a perfect or partial dislocation moves through the crystal lattice. This lattice energy depends on the material and on the crystallographic plane under consideration. In general, the lattice energy $E^{lattice}$ can be written as:

$$E^{lattice} = \sum_{\alpha=1}^{N} \int \phi_\alpha(\zeta_1(\mathbf{x}), \zeta_2(\mathbf{x}), \ldots, \zeta_N(\mathbf{x})) d^2x \tag{6}$$

where $\phi_\alpha(\zeta_1(x), \zeta_2(x), \ldots)$ is a periodic potential and the equation is integrated over the slip plane. It is also possible that this potential could be a function of multiple order parameters from slip systems, $\zeta_1(x), \zeta_2(x) \ldots \zeta_N(x)$.

The time-dependent Ginzburg-Landau (TDGL) equation is used to evolve the total system energy to equilibrium and determine the order parameters corresponding to the equilibrium state. It relates the time variation of the order parameters to the variation in the total system energy with respect to each order parameter α as follows:

$$\frac{\partial \zeta_\alpha(\mathbf{x}, t)}{\partial t} = -L \frac{\delta E(\zeta)}{\delta \zeta_\alpha(\mathbf{x}, t)} \tag{7}$$

where L is related to the convergence speed (or mobility) of the system and has a non-negative coefficient that is constant for all order parameters. For calculations involving multiple order parameters, Eq. (7) becomes a set of N coupled integro-differential equations, where N equals the number of order parameters, that must be solved numerically to evolve the system. Additionally, the solution of this equation requires the use of a Fast Fourier Transform in order to determine the contribution of the strain energy (as shown in Eq. (3)) to the total energy.

2.2. Phase field extensions for HCP crystal structures

The PF formulation for an HCP crystal structure departs from the foregoing one in two main aspects, first by taking into account the low symmetry of the HCP crystal structure, and second, the multiplicity of slip modes. These aspects affect the development of all energetic terms in the master energy functional, which in the present study, are the elastic strain energy, external energy, and lattice energy in Eq. (1).

The first important departure from the cubic systems is that the basis for the lower symmetry HCP system is not Cartesian. Directions in the HCP unit cell are conventionally expressed using the Miller-Bravais four-index notation {hk.l} or Miller three-index notation {hkl}. Unlike FCC metals, the Miller three-index notation for HCP slip systems has a 120° angle between the first two indices. Further one axis, the c-axis, is longer than the other two axes. The c/a ratio depends on the HCP metal. In the present code, we elect to first transform all slip plane normals and slip directions expressed in the HCP basis to a Cartesian coordinate system, so that that usual mathematical manipulations, utilizing dot and cross-products, can be used.

The second aspect concerns the multiplicity of slip modes, which involves specifically appreciating the differences in the atomic structure and crystallography among the common slip modes in the HCP system. Every slip mode in the HCP crystal has its own value of the Burgers vector, slip plane, and number of slip systems. Within a mode, the slip systems share the same crystallography but are independently oriented. Here we demonstrate the method by modeling dislocations on three of the most frequently observed modes in deformed HCP crystals: the basal, prismatic, and pyramidal-II slip modes. Both the basal ((0001) plane) and prismatic ({$\bar{1}010$} type planes) slip modes accommodate glide of $<a>$-type dislocations, which are dislocations with $<a>$ Burgers vectors. The prismatic and basal slip modes also each have three slip systems. The pyramidal-II mode ({$\bar{2}112$} type planes), however, can accommodate strain in the $<c>$ direction through the motion of $<c+a>$ dislocations. The Burgers vector is aligned along a specific $<c+a>$ direction lying in the glide plane. Six slip systems belong to the pyramidal-II mode. Apart from these three modes, a few other slip modes have been observed in the deformation of HCP crystals (such as the pyramidal-I mode) but are not considered in the present examples. These can be incorporated using the same methodology as developed here.

Redefinition of the slip planes and slip directions for the HCP crystal affect the formulation of the plastic strain, ϵ^p, which is used directly in the calculation of the elastic strain energy and external energy, Eqs. (3) and (5). To accommodate the different slip modes and their distinct Burgers vectors, Eq. (4) is re-written to consider a slip plane-dependent Burgers vector:

$$\epsilon_{ij}^p = \frac{1}{2} \sum_{\alpha=1}^{N} b_\alpha \zeta_\alpha(\mathbf{x}, t) \delta_n (s_i^\alpha m_j^\alpha + s_j^\alpha m_i^\alpha) \tag{8}$$

As before, the slip plane normal and slip direction are slip system-dependent, but in the above, the dependency of the magnitude of the Burgers vector on the slip mode is also taken into account. N is the total number of slip planes. Considering the three slip modes, we define N_b, N_{pr}, and N_{py} as the number of slip systems available in the basal, prismatic, and pyramidal-II slip modes, respectively. Hence, $N_b + N_{pr} + N_{py} = N$ and $\alpha = 1$ to N, where $N = 12$.

The expression for $E^{lattice}$ will also differ substantially from one slip mode to another within the same HCP crystal. First, as in the other terms, the crystallography of the slip planes and slip directions associated with preferred slip in the HCP crystal must be defined. Second, the lattice energies for each slip mode need to be considered individually, since the atomic density and configuration of the atoms differ among the glide planes of these modes. The general form of the lattice energy presented in Eq. (6) is still appropriate; however, the functional form of the periodic potential will depend on the atomic interactions across the particular slip plane of interest. The total $E^{lattice}$ will consist of the energy contributions from dislocations that may be present on any or all of these three slip modes at a time.

In the present formulation, slip by each slip system is defined physically and so a unique order parameter is associated with each slip system. Consequently, the lattice energies associated with different systems are mutually exclusive, permitting us to write the lattice energy as follows:

$$E^{lattice} = E^{basal} + E^{prism} + E^{pyrII}$$

$$= \sum_{\alpha=1}^{N_b} \int \phi_\alpha^{basal}(\zeta_1(\mathbf{x}), \ldots, \zeta_{N_b}(\mathbf{x})) d^2x + \sum_{\alpha=1}^{N_{pr}} \int \phi_\alpha^{pr}(\zeta_1(\mathbf{x}), \ldots, \zeta_{N_{pr}}(\mathbf{x})) d^2x + \sum_{\alpha=1}^{N_{py}} \int \phi_\alpha^{pyrII}(\zeta_1(\mathbf{x}), \ldots, \zeta_{N_{py}}(\mathbf{x})) d^2x$$

(9)

where E^{basal} is the lattice energy for dislocations gliding on basal slip planes, E^{prism} the lattice energy for dislocations gliding on prismatic planes, and E^{pyrII} for the lattice energy for dislocations gliding on pyramidal-II planes. At a given point in the computational volume, lattice energies will for the most part correspond to one plane and hence order parameters on that plane. The sum of two or more lattice energies will occur when glide planes from different slip modes intersect. In addition, as exemplified in Eq. (6), the periodic potentials may be a function of order parameters from multiple slip systems.

2.3. DFT Determined γ-surfaces and GSFE curves

The $E^{lattice}$ is a material-specific and slip-plane-specific function of the order parameters, associated with the energy expended when bonds are broken across the plane in dislocation glide. In prior works, the models used for $E^{lattice}$ originate from simple functions, such as a single parameter sine-squared function (Zeng et al., 2016) to multi-parameter piece-wise quadractic function (Koslowski et al., 2002), to more complex sinusoidal functions modeling in detail a generalized stacking fault energy (GSFE) curve (Hunter et al., 2011; Shen and Wang, 2003), or Fourier sine series (Beyerlein and Hunter, 2016; Hunter et al., 2014; Schoeck, 2001; Shen and Wang, 2004), modeling a 2D γ-surface. The parameters associated with these functions are usually informed by an atomistic calculation particular to the material. When the energy landscape is too complex to be described reliably by a function, an alternative approach has been to employ look-up tables comprised a large set of pre-calculated energies corresponding to a fine grid of points on the energetic landscapes (Mianroodi and Svendsen, 2015; Xu et al., 2019). Obtaining the energy associated with dislocation glide on a particular plane has been derived by considering an ideal situation of cutting a perfect crystal in half across the glide plane of interest and calculating the excess energy per unit area incurred by shifting one crystal half with respect to the other half (Schoeck, 2005; Vitek, 1968). The γ-surface is the energy landscape associated with all possible shifts in the two in-plane dimensions. The energy associated with shifting this plane in solely one crystallographic direction lying on the plane (one slice of the γ-surface) corresponds to a curve, referred to as a generalized stacking fault energy (GSFE) curve. In the case of slip in an FCC crystal, γ-surface is usually calculated for the {111} slip plane, the one glide plane of interest, and the energy associated with shifting this plane in either the $<110>$ or $<112>$ directions are the common GSFE curves. GSFE curves and γ-surfaces do not directly represent a dislocation, but they represent the energy associated with the changes in atomic positions that a dislocation would cause as it glides on that plane. These energetic quantities have been adopted in $E^{lattice}$ since they are undeniably more convenient to calculate than the Peierls barrier.

Here, as mentioned, we apply the model to different glide planes in four HCP crystals, Mg, MgY, Ti, and Zr, and we will adopt GSFE curves or γ-surfaces in $E^{lattice}$ for them. These energetic quantities are commonly calculated with atomic-scale methods, such as DFT or MD (Mianroodi et al., 2016; Shen et al., 2014). However, most DFT γ-surfaces and GSFE curves apply to cubic materials and not to planes in HCP materials (Kaxiras and Duesbery, 1993; Lu et al., 2000). The most common cases for HCP metals are the GSFE curves for the basal slip mode in Mg and Mg alloys (Shang et al., 2014; Shen et al., 2014; Wu et al., 2015). Here we will use the GSFE for the basal plane in $Mg_{47}Y$ from Pei et al. (2013). For the prismatic slip plane in Mg, Zr and Ti, the DFT-calculated GSFE curves that we will use have been calculated in (Ardeljan et al., 2018; 2016; Clouet, 2012; Domain, 2006; Wu et al., 2015). The γ-surface for the pyramidal-I plane in Mg has already been presented in (Kumar et al., 2017; Rodney et al., 2017; Wu et al., 2015).

For the PFDD calculations presented in this work, we performed additional DFT calculations for the GSFE curves for the HCP crystalline planes that are not available in the literature, which include γ-surfaces and GSFE curves for the basal plane in Mg and the pyramidal-II planes in Mg and Ti. For all DFT calculations here we use the code as implemented in Vienna *Ab-initio* Simulation Package (VASP) (Kresse and Furthmüller, 1996a; 1996b) and utilize the generalized gradient approximation (GGA) for the exchange correlation functional with the Perdew-Burke-Ernzerhof (PBE) parameterization (Perdew et al., 1996). The interaction between valence electrons and ionic cores was treated using PAW potentials. The number of valence electrons in Mg potential taken is 2 and in the Ti potential 4. A plane wave energy cutoff of 400 eV was employed and the structure was optimized until the force on each atom became smaller than 0.01 eV/A. We used a 19x19x19 Gamma-centered

Table 1
Lattice constant (in Å) and elastic constants (units of GPa) for bulk HCP-Mg, Ti, and Zr obtained from DFT and isotropic averages for the shear modulus, μ, and Lamé's parameter, λ.

Material	a(Å)	c/a	C_{11}	C_{33}	C_{12}	C_{13}	C_{44}	C_{66}	μ	λ
Magnesium	3.190	1.625	63.3	65.7	25.9	20.8	18.0	18.7	19.26	23.53
Mg$_{47}$Y	3.206	1.626	63.3	65.7	25.9	20.8	18.0	18.7	19.26	23.53
Titanium	2.923	1.581	159.4	191.7	108.9	83.9	37.6	25.2	35.68	94.43
Zirconium	3.231	1.601	135.1	166.1	80.3	70.7	26.1	27.4	30.23	77.59

Monkhorst Pack k-point mesh to integrate the Brillouin Zone of the primitive HCP unit cells to calculate the lattice constants and elastic constants.

The lattice parameters and elastic constants are presented Table 1. All values were calculated here using our DFT methods but the moduli for Mg$_{47}$Y, which were obtained from Pei et al. (2013). Overall, these are in good agreement with previous DFT calculations and experimental measurements (Ardeljan et al., 2016; Kumar et al., 2017). These values will be used in the PFDD calculations that follow. For the sake of simplicity, the elastic strain energy generated around the dislocation is calculated under the assumption that the material is a linear elastic, isotropic solid. The isotropic elastic stiffness tensor is given by:

$$
\mathbf{C} = \begin{bmatrix}
\lambda + 2\mu & & & & & \\
\lambda & \lambda + 2\mu & & & & \\
\lambda & \lambda & \lambda + 2\mu & & \text{Symm} & \\
& & & \mu & & \\
& & & & \mu & \\
& & & & & \mu
\end{bmatrix}
\tag{10}
$$

where μ is the shear modulus and λ is Lamé's first parameter, which are related by

$$
K_b = \lambda + \frac{2}{3}\mu
\tag{11}
$$

We calculate μ and K_b using the following Voigt equations for hcp (Hill, 1952)

$$
\mu = \frac{1}{15}[(2C_{11} + C_{33}) - (C_{12} + 2C_{13}) + 3(2C_{44} + C_{66})]
\tag{12}
$$

$$
K_b = \frac{1}{9}[(2C_{11} + C_{33}) + 2(C_{12} + 2C_{13})]
\tag{13}
$$

The DFT determined and isotropic averages used in the calculations for Mg, Ti, and Zr are presented in Table 1.

In the DFT calculation of the generalized stacking fault energies, we used the relaxed method (Kumar et al., 2017), wherein for each displacement step, minimization of the energy of the system is ensured by fixing all atomic positions along the glide direction and allowing positions along the plane normal and the in-plane direction lying normal to the glide direction to relax. For each slip plane, the supercell dimensions are chosen based on the minimum number of layers along the z-direction for which convergence in system energy is attained. For Mg, the periodic model for basal slip plane contains 52 atoms and its dimensions are 3.19 Å along x, 5.53 Å along y and 77.17 Å along z. The periodic model for pyramidal-II slip plane in Ti contains 60 atoms and its dimensions are 5.063 Å along x, 5.467 Å along y, and 51.960 Å along z. All supercells contain a thick vacuum layer of 15 Å along the z-direction.

2.4. The lattice energy for the basal slip mode

On the basal plane, there are three possible directions of slip, each corresponding to an order parameter for that plane, ζ_1, ζ_2, and ζ_3. For the basal plane, the lattice energy E^{basal} can be expressed as:

$$
E^{basal} = \sum_{\alpha=1}^{N_b} \int \phi_\alpha^{basal}(\zeta_1, \zeta_2, \zeta_3) d^2x,
\tag{14}
$$

where ϕ_α^{basal} is the periodic potential and $\alpha = 1$ to N_b, the number of basal slip systems. As mentioned, here we characterize this potential with the GSFE surface, or γ-surface, the excess energy associated with shift one crystalline half relative to another about the basal plane. Using DFT for set of in-plane shear displacement, this surface has been calculated for Mg. Fig. 1 presents the γ-surface for the basal plane calculated from DFT. First, it is recognized that the location of the maxima and minima in this basal plane γ-surface coincide well with those of the {111} plane in an FCC crystal. In prior PFDD work on FCC γ-surfaces, a common approach is to parameterize a continuous function for the $\phi(\zeta)$ from a discrete set of DFT calculations on a γ-surface. In this way derivatives were directly calculable and less DFT calculations were required overall to construct the potential. A function that fit the FCC plane well is the seven-coefficient complex Fourier series function
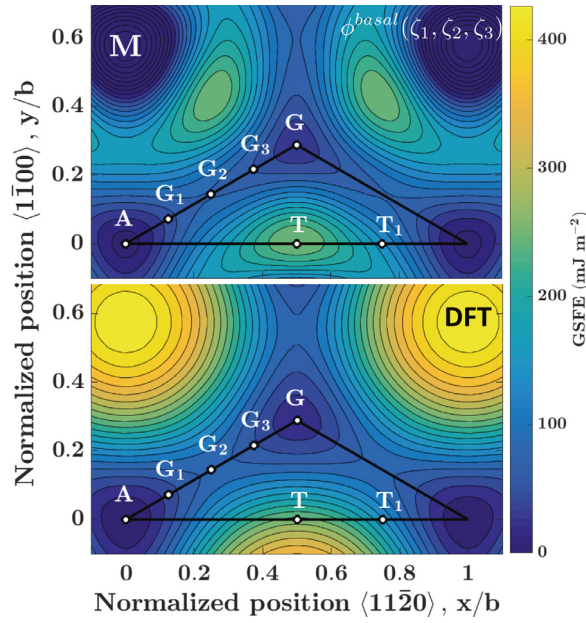
Fig. 1. Comparison of γ-surfaces for the basal slip plane in Mg as determined with DFT (bottom) and the parameterization (top) presented in Eq. (15). The points used from the material γ-surface to determine the coefficients calculated with Eq. (16) are labeled on both plots.

(Hunter et al., 2014; Schoeck, 2001; Shen and Wang, 2004). Here we adopt this function for the ϕ_α^{basal} and parameterize it for the basal plane using the seven DFT calculated points on the basal plane γ-surface. This function is given by:

$$
\begin{aligned}
\phi^{basal}(\zeta_1, \zeta_2, \zeta_3) = & \, j_0 + j_1[\cos 2\pi (\zeta_1 - \zeta_2) + \cos 2\pi (\zeta_2 - \zeta_3) + \cos 2\pi (\zeta_3 - \zeta_1)] \\
& + j_2[\cos 2\pi (2\zeta_1 - \zeta_2 - \zeta_3) + \cos 2\pi (2\zeta_2 - \zeta_3 - \zeta_1) + \cos 2\pi (2\zeta_3 - \zeta_1 - \zeta_2)] \\
& + j_3[\cos 4\pi (\zeta_1 - \zeta_2) + \cos 4\pi (\zeta_2 - \zeta_3) + \cos 4\pi (\zeta_3 - \zeta_1)] \\
& + j_4[\cos 4\pi (3\zeta_1 - \zeta_2 - 2\zeta_3) + \cos 4\pi (3\zeta_1 - 2\zeta_2 - \zeta_3) \\
& + \cos 4\pi (3\zeta_2 - \zeta_3 - 2\zeta_1) + \cos 4\pi (3\zeta_2 - 2\zeta_3 - \zeta_1) \\
& + \cos 4\pi (3\zeta_3 - \zeta_1 - 2\zeta_2) + \cos 4\pi (3\zeta_3 - 2\zeta_1 - \zeta_2)] \\
& + k_1[\sin 2\pi (\zeta_1 - \zeta_2) + \sin 2\pi (\zeta_2 - \zeta_3) + \sin 2\pi (\zeta_3 - \zeta_1)] \\
& + k_3[\sin 4\pi (\zeta_1 - \zeta_2) + \sin 4\pi (\zeta_2 - \zeta_3) + \sin 4\pi (\zeta_3 - \zeta_1)],
\end{aligned}
\tag{15}
$$

where the coefficients $j_0 - j_4, k_1, k_3$ define the material-dependent local maximum, local minimum, and curvature of the 2D energy surface. These coefficients correspond to particular points taken from the γ-surface, G, G_1, G_2, G_3, T, T_1 and are related to the coefficients via the following expressions (Schoeck, 2001):

$$
\begin{aligned}
j_0 &= 0.823(4G - 6G_1 + 6G_2 - 7.392G_3 + 0.804T + 0.804T_1) \\
j_1 &= 0.274(-8G + 12G_1 - 12G_2 + 14.785G_3 - 1.608T + 0.215T_1) \\
j_2 &= 0.091(23.072G - 29.138G_1 + 32.785G_2 - 42.215G_3 + 2.569T - 2.412T_1) \\
j_3 &= 0.137(-8G + 12G_1 - 12G_2 + 14.785G_3 + 0.215T - 1.608T_1) \\
j_4 &= 0.023(1.856G - 13.723G_1 + 6.431G_2 - 4.277G_3 - 0.962T + 3.531T_1) \\
k_1 &= 0.137(-32G + 48G_1 - 48G_2 + 62.785G_3 - 4.608T - 2.785T_1) \\
k_3 &= 0.046(17.072G - 19.292G_1 + 31.923G_2 - 34.708G_3 + 3.341T - 8.354T_1).
\end{aligned}
\tag{16}
$$

Fig. 1 compares the DFT calculated γ-surface for pure Mg and the surface calculated with the Fourier series approximation presented in Eq. (15). The points, G, G_1, G_2, G_3, T, T_1, taken from the γ-surface to parameterize the approximation, are also shown on both energy landscapes. The pathway starting at point A and traveling through points T and T_1 (in $< 11\bar{2}0 >$ type directions) represents a perfect Burgers vector translation. The other two pathways (one starting at A and traveling through G_1, G_2, G_3 to point G, and the other starting at point G), represent the two partial dislocation translations in $< 1\bar{1}00 >$ type directions. In the case of basal slip, the six points shown in Fig. 1 from the material γ-surface determine the coefficients needed in Eq. (15). These values for pure Mg are: $G = 29.32 \ mJ/m^2$, $G_1 = 57.70 \ mJ/m^2$, $G_2 = 88.49 \ mJ/m^2$, $G_3 = 66.08 \ mJ/m^2$, $T = 262.73 \ mJ/m^2$, and $T_1 = 151.53 \ mJ/m^2$. The greatest deficiency of the Fourier series approximation is

Table 2
Inter-planar spacing d normalized in terms of the Burgers vector b and the calculated coefficients for the lattice energy potential function (Eq. (15)) for the basal slip mode. All coefficients are shown in units of mJ/m^2.

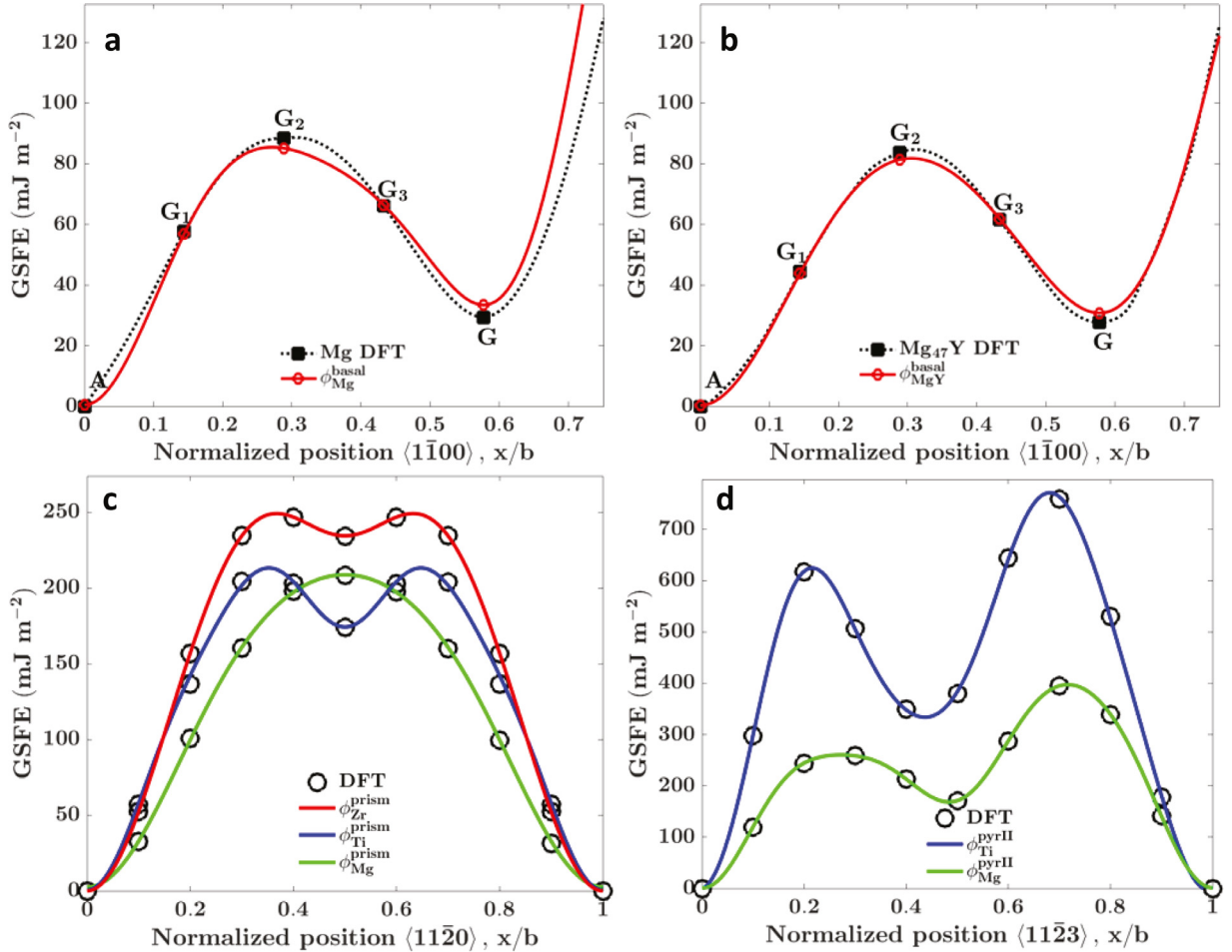| Material	d	j_0	j_1	j_2	j_3	j_4	k_1	k_3
Mg	0.81250	120.7223	−4.6751	−53.0878	25.4338	−3.8782	13.6261	−21.5761
Mg$_{47}$Y	0.81305	143.6364	−33.1868	−18.2934	5.6344	−0.9729	−44.8569	−6.2832

Fig. 2. Direct comparison of GSFE curves determined with DFT and the periodic potentials used in the calculation of the lattice energy in PFDD for (a) basal slip systems in pure Mg, (b) basal slip systems in Mg$_{47}$Y, (c) prismatic slip systems in pure Mg, Zr, and Ti, and (d) pyramidal-II slip systems in pure Mg, and Ti. Unlike the symmetric energetic paths for partials on the basal and prismatic planes, the pyramidal-II plane can have different positions and values for the local minima and maxima.

labeled by M in the top figure of Fig. 1. The M point represents a global energetic maximum where two atoms are located directly on top of each other, and is incorrectly represented by Eq. (15). However, this atomic configuration is not located along a pathway that would be involved in the dissociation of the perfect dislocation.

In order to model basal slip in Mg$_{47}$Y, we determined a parameterized γ-surface from the same seven points lying along the $< 11\bar{2}0 >$ and $< 1\bar{1}00 >$ GSFE curves calculated by DFT by Pei et al. (2013). From their work, we obtained the following values for Mg$_{47}$Y: $G = 27.80 \ mJ/m^2$, $G_1 = 44.46 \ mJ/m^2$, $G_2 = 83.82 \ mJ/m^2$, $G_3 = 61.65 \ mJ/m^2$, $T = 214.69 \ mJ/m^2$, and $T_1 = 124.34 \ mJ/m^2$. Using these values in Eq. (16), the coefficients needed to inform ϕ^{basal} are calculated and presented in Table 2. Fig. 2(a) and (b) directly compare the GSFE curves in a $< 1\bar{1}00 >$ type direction as determined with DFT and the Fourier series approximation, showing reasonable agreement for this particularly important slice of the energetic landscape.

2.5. The lattice energy for the prismatic and pyramidal-II slip modes

For prismatic slip, the relevant GSFE curve on the prismatic plane is associated with the prismatic slip system, $\{\bar{1}010\}$ $< 1\bar{2}10 >$. For a prismatic dislocation in PFDD, E^{prism} can be expressed as a function of a single order parameter ζ_α corre-

Table 3

Inter-planar spacing d normalized in terms of the Burgers vector b and the calculated coefficients for the lattice energy periodic potentials for the prismatic and pyramidal-II (Eq. (19)) slip mode. All coefficients are shown in units of mJ/m^2.

Material	Plane	d	p_0	p_1	p_2	p_3	p_4	q_1	q_2	q_3	q_4
Mg	Prism	0.86603	119.18	−102.05	−13.60	−1.117	0.000	0.000	0.000	0.000	0.000
Ti	Prism	0.86603	138.65	−89.53	−43.96	2.591	−7.328	0.000	0.000	0.000	0.000
Zr	Prism	0.86603	129.90	−93.28	−33.45	3.198	−4.051	0.000	0.000	0.000	0.000
Mg	Pyr II	0.22318	217.98	−75.35	−116.48	−6.137	−9.728	−55.26	15.05	8.900	−1.228
Ti	Pyr II	0.22589	427.52	−165.06	−220.30	−22.96	−9.542	−52.33	118.72	−13.57	−16.63

sponding to the slip direction $< 1\bar{2}10 >$ on the prismatic plane. The lattice energy is given by:

$$E^{prism} = \sum_{\alpha=1}^{N_{pr}} \int \phi_\alpha^{prism}(\zeta_\alpha) d^2x, \tag{17}$$

ϕ_α^{prism} is the periodic potential for the excess energy expended in gliding along the slip vector. The ϕ_α^{prism} can be characterized by a GSFE curve along the slip direction $< 1\bar{2}10 >$. Here, these GSFE curves are calculated by DFT and are taken from published DFT results from Ardeljan et al. (2018) for Mg, Ardeljan et al. (2016) for the Zr data, and Domain (2006) for the Ti data. Fig. 2(c) displays these curves. In a material like Zr, the GSFE curve along the prismatic plane has a local minimum, suggesting the possibility of a dislocation dissociation. Conversely in Mg, the GSFE curve has no local minimum, which would imply that the core is likely to remain compact.

The relevant GSFE curve for the pyramidal-II slip system is $\{\bar{2}112\} < 2\bar{1}\bar{1}3 >$. Similar to the prismatic case, we consider only one active order parameter ζ_α defined in a $< 2\bar{1}\bar{1}3 >$-type slip direction. In this case, the lattice energy is given by:

$$E^{pyrII} = \sum_{\alpha=1}^{N_{py}} \int \phi_\alpha^{pyrII}(\zeta_\alpha) d^2x, \tag{18}$$

where ϕ^{pryII} is the periodic potential associated with excess energy in gliding along the slip vector. For ϕ^{pryII}, we adopt a generalized stacking fault energy curve along $< 2\bar{1}\bar{1}3 >$ calculated using DFT. The pyramidal plane GSFE curve for Mg is taken from Kumar et al. (2017), but here, it was necessary to calculate the GSFE curve for Ti, as described in Section 2.3. GSFE curves for both Mg and Ti are different from those DFT curves previously reported, which did not employ full relaxation (Rodney et al., 2017; Wu et al., 2015).

In an effort to provide a continuous function for ϕ, we observe that the DFT GSFE curves for the prismatic and pyramidal-II systems for the particular metals we study here can be generally represented by the following function (where we drop the subscript α on ζ for brevity):

$$\begin{aligned} \phi^m(\zeta) = {} & p_0 + p_1 \cos(2\pi\zeta) + p_2 \cos(4\pi\zeta) + p_3 \cos(6\pi\zeta) + p_4 \cos(8\pi\zeta) \\ & + q_1 \sin(2\pi\zeta) + q_2 \sin(4\pi\zeta) + q_3 \sin(6\pi\zeta) + q_4 \sin(8\pi\zeta), \end{aligned} \tag{19}$$

where $m = prism$ and/or $pyrII$ depending on the active slip mode(s). We found this function convenient, but emphasize that not all GSFE curves would require all nine coefficients. If the potential is symmetric, such as for the prismatic plane GSFE curve for Ti, then the coefficients $q_1 - q_4$ can be set to zero. If it is symmetric and contains no local minima, like the prismatic plane GSFE curve for Mg, then p_4 can also be equal to zero.

The parameterized curves for ϕ_α^{prism} are compared against the DFT calculations in Fig. 2(c). In these three metals, the continuous potential function provides excellent agreement to the data. Fig. 2(d) shows the DFT calculated pyramidal-II GSFE curves in comparison with the function in Eq. (19) for Mg and Ti. The pyramidal-II plane has an asymmetric GSFE curve along the slip direction, which requires calculation of all $p_0 - p_4, q_1 - q_4$ coefficients to fit the potential ϕ_α^{pyrII} to the DFT determined energy profile. For the two pyramidal-II curves, the function offers an excellent continuous function representation to the DFT data. All coefficients for the prismatic and pyramidal-II cases were fit using the MATLAB curve fitting tool (MATLAB and Curve Fitting Toolbox Release, 2016b) and they are summarized in Table 3.

3. Equilibrium dislocation structure calculations

In the following sections, we apply the HCP-PFDD method to simulate the dissociation of an initially perfect dislocation into a stable, equilibrium structure under zero applied stress. The structural characteristics that can be ascertained from the calculation are the partial dislocations resulting from the dissociation, the distance between the partials, the width of the individual partials and any asymmetry between their widths. For demonstration, the character of the starting perfect dislocation will be either pure edge or pure screw, although in principle, a dislocation of any initial character may be considered. In the examples, these dislocations lie on one of three planes: basal, prismatic, and pyramidal-II. When possible, we compare our results to those previously calculated by DFT and molecular statics or MD. Not all cases treated here have been observed experimentally or pursued by other computational methods, such as DFT or MD.
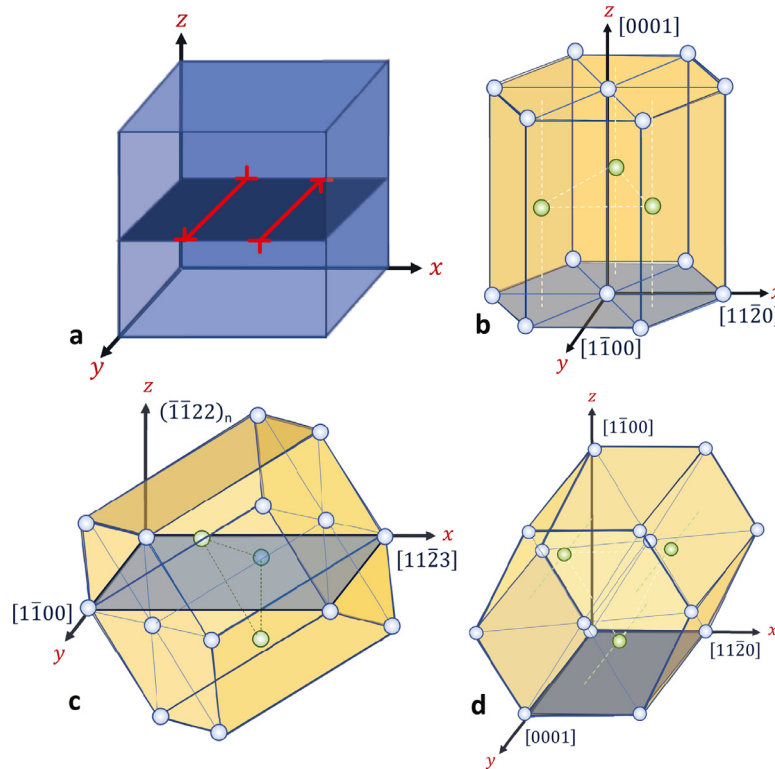
Fig. 3. Schematics showing (a) the initial simulation set-up for the PFDD computational cell, which was utilized with orientations for an edge dislocation on the (b) basal, (c) pyramidal-II, and (d) prismatic glide planes. The simulation set-up for a screw dislocation would have the same initialization shown in (a), while the unit cells in (b–d) would be rotated around their respective $z-axis$ by 90°. For clarity, the $x-$, $y-$, and $z-axis$ in our simulation cell correspond to the $x-$, $y-$, and $z-axis$ respectively in our unit cells when initializing for an edge dislocation and to $y-$, $x-$, and $z-axis$ respectively when initializing for a screw dislocation. Thus, the slip plane lies parallel to the simulation cell surface, the dislocation line sense lies parallel to the $y-axis$ and the Burgers vector (and unit cell) orientation is reflective of the desired dislocation character).

3.1. Simulation configuration

All simulations were carried out in a 3D cuboidal simulation cell. Due to the use of a Fourier transform in the calculation of the elastic strain energy, all boundaries are periodic. We elect to orient the primary glide plane such that its normal direction lies parallel to the z-axis, as shown in Fig. 3(a). Accordingly the crystallographic directions of the x, y, and z-directions depend on the slip system of interest. The corresponding directions for each simulation cube used for the basal, prismatic, and pyramidal-II planes are shown for an edge dislocation in Fig. 3(b), (c), and (d), respectively. The $x-$, $y-$, and $z-axis$ in our simulation cell Fig. 3(a) correspond to the $x-$, $y-$, and $z-axis$ respectively in our unit cells (see Fig. 3(b-d)) when initializing for an edge dislocation and to $y-$, $x-$, and $z-axis$ respectively when initializing for a screw dislocation. Thus, the slip plane normal is always parallel to the $z-axis$ of the simulation cell, the dislocation line sense is always parallel to the $y-axis$ and the Burgers vector, which determines the orientation of the unit cell within the simulation cell and the character of the dislocation with respect to the line sense, is parallel to the $x-axis$ for an edge dislocation and the $y-axis$ for a screw dislocation. This additional orientation step is not a requirement but a choice made here since only one dislocation is being evaluated at a time in this study.

For convenience the grid spacing in all x, y, and z directions, is chosen to be the inter-planar distance of the slip plane, d, (normalized by the Burgers vector b of a dislocation on that plane for a material, given in Tables 2 and 3. For any HCP slip plane, given in $(hkil)$ or $(hk.l)$ Miller-Bravais notation the un-normalized inter-planar spacing d_* depends on the c/a ratio, and is given by $\frac{1}{d_*^2} = \frac{4}{3}\frac{h^2+hk+k^2}{a^2} + \frac{l^2}{c^2}$. In this way, the c-axis, and in particular, differences in the c-axis length (or the c/a ratio) for different HCP materials are taken into account. For the particular set up chosen here, the c-axis length is taken into account in the grid spacing normal to the slip plane (z-axis in Fig. 3(a)). Accounting for the c-axis in this way is advantageous when using a cubic computational grid, as is done here. A computational cell length of $D = 256d$ was used for simulations on basal and prismatic planes, and $D = 640d$ was used for simulations modeling the pyramidal-II plane. By repeating the simulation for different cell sizes, the cell sizes used for the results that follow were determined to be sufficiently large that the dislocation structures were unaffected by the image dislocations in the periodic cells.
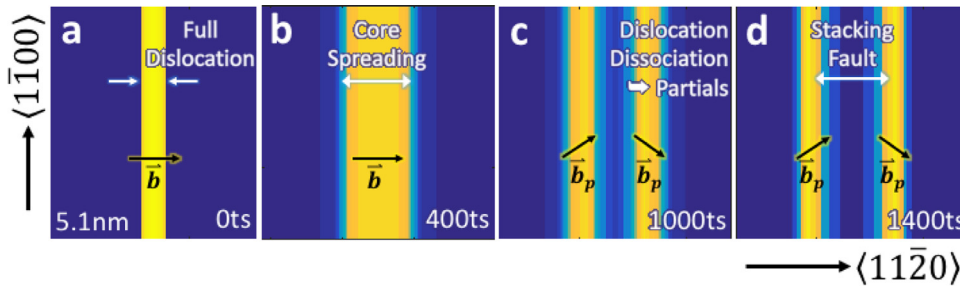
Fig. 4. Zoomed-in area of the slip plane showing the gradient of the disregistry $d\Delta/dx$ from PFDD for a basal edge dislocation in Mg as it evolves to a final equilibrium dissociated state over time: (a) 0, (b) 400, (c) 1000, and (d) 1400 time steps. The approximate side length of the area shown is 5.1 nm. The arrows labeled b and b_p are the Burgers vectors for the full and partial dislocations respectively.

Inside the crystal, a dislocation dipole, consisting of a pair of perfect dislocations with equal and opposite sign, is initially placed on the glide plane (see Figs. 3(a) and 4(a,c)). The dipole allows for a zero Burgers circuit around the simulation cell. The calculations are completed for both a perfect edge dipole and a perfect screw dipole. For the edge case, the line orientation is aligned along the y-axis and the Burgers vector along the x-axis. For the screw dipole, the line orientation is aligned along the y-axis and Burgers vector also along the y-axis. With the perfect dislocations in place on the glide plane, the simulation begins by evolving the system energy using Eq. (7) to a minimum energy state. During this time, we observe that in some cases a perfect dislocation dissociates into smaller partial dislocations, which move apart in the glide plane, while in other cases, the dislocation simply spreads but does not dissociate. Since no external stress is applied in the examples here, the partial dislocations move to achieve an equilibrium structure.

To identify the displacement resulting from dislocation glide, particularly when multiple order parameters are active, we calculate the disregistry $\Delta(x)$ across the glide plane, which is defined as (Shen and Wang, 2004)

$$\Delta(x) = \sum_{i=1}^{3} \zeta_i(x) s_i \cdot s_p, \tag{20}$$

where s_p is the Burgers vector direction of the initial perfect dislocation, and s_i are the slip directions of each order parameter ζ_i on the glide plane. For instance, in the case of the basal plane, there are three order parameters, ζ_1, ζ_2, and ζ_3 (in directions $[11\bar{2}0]$, $[1\bar{2}10]$, $[\bar{2}110]$). Slip directions of Shockley partial dislocations ($[\bar{1}100]$, $[0\bar{1}10]$, $[10\bar{1}0]$) would correspond to a linear combination of ζ_1, ζ_2, and ζ_3, see Eq. (15). A dislocation is located at the boundary where the disregistry $\Delta(x)$ transitions from 0 to 1 (see Fig. 4(a,b)).

A dislocation results in a gradient in $\Delta(x)$. The peak in $d\Delta(x)/dx$ corresponds the central position of a dislocation and spread non-zero $d\Delta(x)/dx$ about the peak corresponds to its width (see Fig. 4(c,d)). Splitting of the perfect dislocation into multiple partial dislocations of smaller Burgers vector values would correspond to multiple peaks in the final $d\Delta(x)/dx$ profile, the distance between which is quantified as the stacking fault width SFW. In the case, where the perfect and partial dislocations are collinear (i.e., only one order parameter is active), the disregistry (Δ), calculated in Eq. (20), is equivalent to the order parameter (ζ). To best visualize important structural features of the relaxed dislocations and any resulting partials and SFW we plot a zoomed in cross-section, centered around the position of the initial perfect dislocation, for both the disregistry $\Delta(x)$ and the gradient of the disregistry $d\Delta/dx$.

3.2. Dissociation on the basal plane

With the PFDD model, we simulate the dissociation of perfect edge and screw oriented dislocations along the basal plane in pure Mg. Fig. 5 shows the disregistry $\Delta(x)$ profile of the final state of the edge and screw basal dislocation after the dissociation has completed. To reveal the dislocations, in the same figure, the gradient $d\Delta(x)/dx$ is also presented.

The calculation predicts that both edge and screw dislocations split into two Shockley partials, which correspond to the two peaks in the $d\Delta(x)/dx$ curve. The spread about these peaks indicates the widths of the partials, which are observed to be nearly equal. The stacking fault width (SFW) is the distance between these peaks or the center-to-center distance between the partials. Due to the grid spacing used in the PFDD calculations the error in the SFW is $\pm$ 0.5d. As defined, a portion of the SFW includes the cores of the partials and is not comprised entirely of a perfect intrinsic stacking fault. For an edge dislocation in the basal plane of pure Mg, the SFW is 15.551 Å (4.875b), where $b = 3.190$ on the basal plane for Mg. For the screw dislocation, the SFW is 10.367 Å (3.250b). The dissociation of perfect edge and screw basal dislocations in Mg$_{47}$Y are also simulated and the results included in Fig. 5 for comparison. The edge dislocation dissociation results in a SFW of 20.856 Å (6.504b), and the screw dislocation dissociation, a SFW of 10.428 Å (3.2522b), where $b = 3.2064$ on the basal plane for Mg$_{47}$Y. The differences in the SFWs between Mg and Mg$_{47}$Y are negligible for the screw dislocation and ~ 5 Å, just slightly less than 2b, wider for an edge dislocation on Mg$_{47}$Y compared to Mg. It can also be seen from $d\Delta/dx$ that
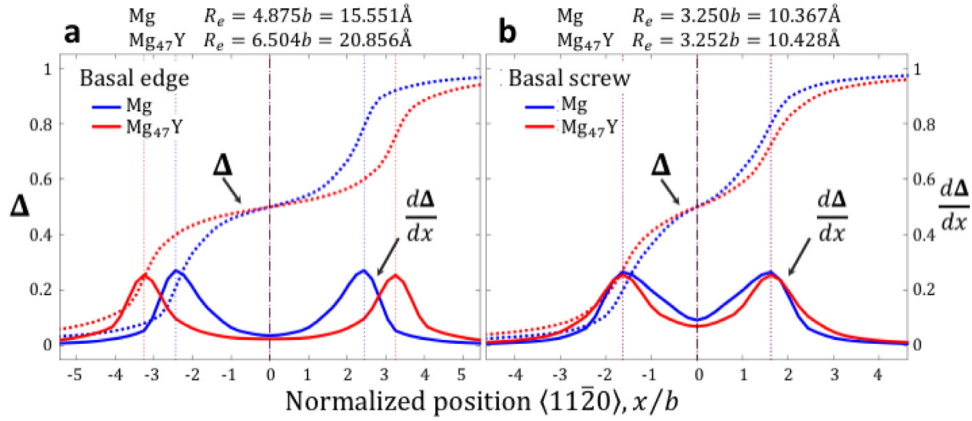
Fig. 5. Equilibrium stacking fault width calculations for initially (a) edge and (b) screw oriented perfect dislocations in the basal plane as determined by PFDD. Results for both pure Mg and Mg$_{47}$Y are shown.

the cores of the two partials are narrower for Mg$_{47}$Y compared to those for Mg and from $\Delta(x = 0)$ that the magnitude of the Burgers vectors for both the right and the left partials are equal.

The PFDD calculation follows the general expectation from continuum dislocation theory, which is that a perfect dislocation on the basal slip plane undergoes a planar dissociation following (Partridge, 1967):

$$\frac{1}{3}[1\bar{2}10] \rightarrow \frac{1}{3}[1\bar{1}00] + \frac{1}{3}[0\bar{1}10]. \tag{21}$$

The above reaction indicates that a perfect dislocation will dissociate into two Shockley partial dislocations. Analogous to the dissociation of a perfect FCC dislocation on the {111} plane, the Burgers vectors of these Shockley partial dislocations on the basal plane are non-collinear and correspond to the two $< 1\bar{1}00 >$-type directions the basal γ-surface leading to the local minimum (Hirth and Lothe, 1968; Partridge, 1967; Rodney et al., 2017). A force balance on this dissociated structure gives as the split distance, R_e, from the following analytical equation (Hirth and Lothe, 1968)

$$R_e = \frac{\mu}{2\pi\gamma_I}\left[(b_L \cdot \xi_L)(b_T \cdot \xi_T) + \frac{(b_L \times \xi_L)\cdot(b_T \times \xi_T)}{1-\nu}\right], \tag{22}$$

where γ_I is the intrinsic SFE, ν is Poisson's ratio, and b_L and b_T are the Burgers vectors of the leading and trailing partial dislocations, respectively. This expression presumes the reaction has already happened, reached the local minimum configuration, and does not consider the dissociation process that achieved it. Therefore, the only energy on the γ-surface needed is the γ_I, intrinsic stacking fault energy corresponding to the local minimum. This analytical model for Mg basal edge and screw dislocations predicts equilibrium SFW values of 27.360 Å (8.577b) and 13.316 Å (4.174b), respectively. Similarly, in the case of Mg$_{47}$Y, the analytical model produces 27.018 Å (8.443b) for the equilibrium SFW for the split edge dislocation, and 13.15 Å (4.109b) for the split screw dislocation. In both materials, the analytical model overestimates the SFW compared to the PFDD model, which calculated the equilibrium SFW in Mg to be 15.551 Å (4.875b) and 10.367 Å (3.25b) and in Mg$_{47}$Y to be 20.856 Å (6.504b) and 10.428 Å (3.252b) for dissociated edge and screw dislocations respectively. The PFDD simulation takes into account the changes in interaction and lattice energies as the partials glide apart during the dissociation process towards its final equilibrium state, which is not known or specified *a priori*. The analytical model, in contrast, assumes an end state comprised of two distinct partial dislocations and does not account for changes in the interaction energy as the two partial dislocations move apart from each other.

Other computational approaches have been used to calculate the equilibrium structure of the basal dislocation. We compare these results with the PFDD calculations of the equilibrium SFWs for both edge and screw dislocations on the basal plane in pure Mg in Table 4. Atomic-scale simulation has been used to simulate the dissociation process, considering dynamical forces in the disassociation process, which are missing in the PFDD simulation. The data among the atomistic studies are wide spread, due to the use of different simulation cell sizes, boundary conditions, and interatomic potentials. Nevertheless, the PFDD results lie in well within this range. The SFWs reported here are notably close to DFT predictions from Yasi et al. (2009) and Yin et al. (2017). Our results agree well with those from the atomistic study by Shen et al. (2014), who unlike the others in the table used the Mg EAM potential by Daw and Baskes (1984). Values for SFWs calculated by Wu et al. (2015), using both DFT and simulations using the MEAM potential, are the lowest compared to all published DFT and EAM values. We also show estimates form GPN models, which utilize a time-dependent minimization scheme similar to the one used here. Differences between our results and GPN can be attributed to the functional form and origin of the fault energies used in the development of the $E_{lattice}$ term. Our results can be directly compared to the GPN model by Wang et al. (2010), wherein they also used as input a full γ-surface.

Table 4
Equilibrium stacking fault widths in units of Å from the dissociation of edge and screw oriented perfect dislocations along the basal plane in pure Mg reported previously in the literature and compared to values calculated with PFDD. The different methods are abbreviated as: phase field dislocation dynamics (PFDD), density functional theory (DFT), atomistic calculations that use an embedded atom method (EAM) or a modified embedded atom method (MEAM) interatomic potential, Generalized Peierls-Nabarro (GPN), and anisotropic linear elastic theory (ALET). In the PFDD calculations, the error bars correspond to 0.5d, which is error due to the grid spacing used in the calculations.

| Author	Edge (Å)	Screw (Å)	b (Å)	Method
This work	15.551 ± 1.296	10.367 ± 1.296	3.19	PFDD
	27.360	13.316		Analytical (Hirth and Lothe, 1968)
Yasi et al. (2009)	16.64	6.4	3.2	DFT
	14.4	6.4		EAM
	12.8	1.28		EAM
Yin et al. (2017)	23.895	11.151	3.186	ALET
	22.323	12.756	3.189	DFT
Wu et al. (2015)	7.011	4.016	3.187	DFT
	12.493	4.016	3.187	MEAM
Fan et al. (2014)	27.2	14.016	3.2	P-N
Shen et al. (2014)	18.816	6.912	3.2	EAM
Groh et al. (2009)	25.6	16.416	3.2	EAM
Wang et al. (2010)	21.312	–	3.2	GPN
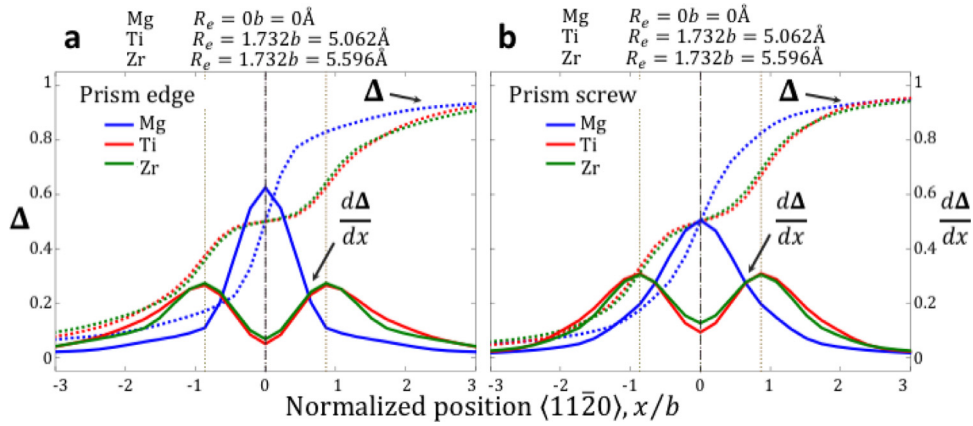
Fig. 6. Equilibrium stacking fault width calculations for initially (a) edge and (b) screw oriented perfect dislocations in the prismatic plane as determined by PFDD. Results for pure Mg, Zr, and Ti are shown.

3.3. Dissociation on the prismatic plane

We next apply the extended PFDD model to dislocations belonging to the prismatic slip mode. Fig. 6 shows the disregistry $\Delta(x)$ and its gradient $d\Delta/dx$ profiles across the final equilibrium dislocation structure for Mg, Zr, and Ti. In the case of Mg, neither the edge nor screw dislocation dissociated, and no stacking fault region develops. The compact structure of the perfect dislocation is maintained. Stability of the compact core can be expected since the GSFE curve for Mg on the prismatic plane lacks a local minimum. This result agrees with DFT and atomistic calculations (Wu et al., 2015). For Zr and Ti, the results from PFDD in Fig. 6 indicate that the perfect dislocations dissociate into two distinct partial dislocations.

In the case of Zr and Ti, both perfect edge and screw dislocations dissociate into two partials, collinear of the [1$\bar{2}$10] type and equal in Burgers vector. The final equilibrium SFW is 5.596 Å (1.732b) for Zr and 5.062 Å (1.732b) for Ti. Neither metal exhibits a strong edge/screw character dependence. The differences between the screw and edge SFW are small and must lie within ± 0.5d, hence significant differences are not apparent in the PFDD calculations. The structures of these dislocations are symmetric, with the cores of the partials being equal in width. In both metals, the SFW is not broad, an outcome of the shallow local energy minimum associated with formation of the stacking fault as seen in the prismatic GSFE curve Fig. 2(c). Further the core widths of the partial dislocations are relatively large compared to the SFW, suggesting that the SFW is not comprised of a homogeneous intrinsic stacking fault. For these dislocations the two partials are slightly more separated in Ti than Zr. The variations arise because the final split distances are influenced by both the repulsive elastic interactions between the partials and the local maxima and minimum in the GSFE curves. Ti has the lower peak barriers, which would lead to the wider partial cores, and it also has the higher modulus, which would lead to the stronger repulsive interaction.

From continuum dislocation theory, perfect dislocations on the prismatic slip plane are expected to dissociate following (Partridge, 1967; Rodney et al., 2017):

$$\frac{1}{3}\left[1\bar{2}10\right] \rightarrow \frac{1}{6}\left[1\bar{2}10\right] + \frac{1}{6}\left[1\bar{2}10\right]. \tag{23}$$

Table 5
Equilibrium stacking fault widths in units of Å from the dissociation of screw oriented perfect dislocations along the prismatic plane in pure Zr reported previously in the literature and compared to values calculated with PFDD. The different methods are abbreviated as: phase field dislocation dynamics (PFDD), anisotropic linear elastic theory (ALET), and semidiscrete variational Peierls-Nabarro (SVPN). In the PFDD calculations, the error bars correspond to 0.5*d*, which is error due to the grid spacing used in the calculations.

Author	Screw (Å)	b (Å)	Method
This work	5.596 ± 1.399	3.231	PFDD
	6.071		Analytical (Hirth and Lothe, 1968)
Clouet et al. (2015)	6.1	3.23	ALET
Udagawa et al. (2010)	17.5	3.23	SVPN

As we have seen from the PFDD calculations, this dissociation is seen only to occur in Zr and Ti and not in Mg. Applying the analytical formula, Eq. (22), to Zr and Ti only and using the energy minimum in the DFT GSFE curves for γ_I, the equilibrium SFWs for an edge and screw dislocation in Zr and Ti are found to be much larger than those calculated by PFDD. For Zr, the analytical model predicts an SFW of 9.730 Å (3.011*b*) for edge and 6.071 Å (1.879*b*) for screw. For Ti, the SFW values are 10.282 Å (3.518*b*) and 6.370 Å (2.179*b*) for edge and screw, respectively. The PFDD simulation takes into account the changes in interaction and lattice energies as the partials glide apart during the dissociation process towards its final equilibrium state. The analytical model, in contrast, neglects the dissociation process.

Transmission electron microscopy (TEM) analyses of Ti and Zr suggest that screw dislocations encounter much higher Peierls barriers than non-screw dislocations, and therefore, control plastic deformation (Farenc et al., 1993; 1995; Naka et al., 1988). Published estimates for the equilibrium SFWs have focused on screw and not edge dislocations. Previous work has computed SFWs for screw dissociations on the prismatic plane in Zr using a P-N model (Clouet, 2012; Domain and Besson, 2004; Udagawa et al., 2010). When these models are informed with DFT values for the elastic constants and γ_I, the calculations are consistent with those calculated here with PFDD (e.g., 5.9 Å and 4.6 Å reported by Clouet (2012)). Other numerical approaches include anisotropic linear elastic theory (ALET) and semidiscrete variational Peierls-Nabarro (SVPN) and these are listed in Table 5. The ALET model (Clouet et al., 2015) achieves reasonable agreement with PFDD, which can be expected since both approaches were informed with DFT. The SVPN result (Udagawa et al., 2010), however, is noticeably higher, since the system minimization is time independent, and like the analytical model, does not consider the dissociation process.

3.4. Dissociation on the pyramidal-II plane

We repeated the equilibrium SFW calculation with PFDD for dissociation of edge and screw dislocations on the pyramidal-II slip plane in Mg and Ti. The GSFE curves along the pyramidal-II slip plane have a local minimum, and we expect two collinear partial dislocations with Burgers vector in a $< 11\bar{2}3 >$ direction to form. Fig. 7 shows the disregistry profiles resulting from the PFDD simulations for edge/screw dissociation in both Mg and Ti. The calculations indicate that two distinct partial dislocations form in both Mg and Ti during the PFDD simulations. For Mg, PFDD simulations calculated equilibrium SFWs of 25.810 Å (4.240*b*) and 19.018 Å (3.125*b*) for perfect edge and screw dislocation dissociation, respectively. In the case of Ti, PFDD calculations produce equilibrium SFWs of 17.293 Å (3.162*b*) and 11.117 Å (2.033*b*) for edge and screw dislocation dissociation, respectively.
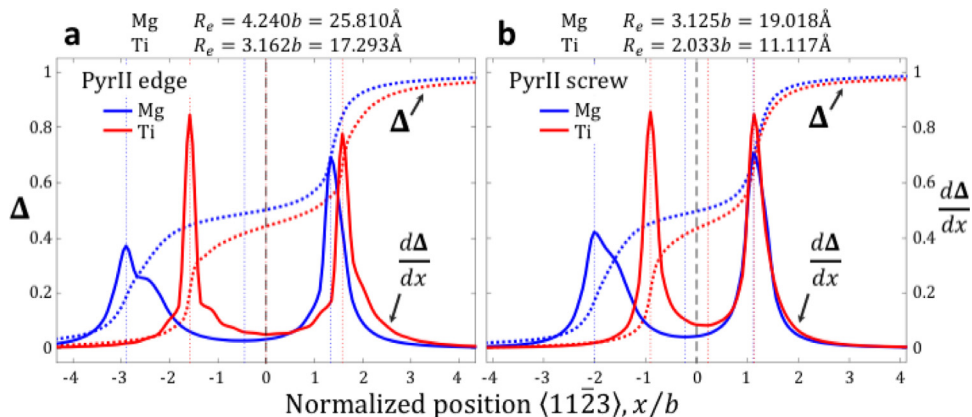

Fig. 7. Equilibrium stacking fault width calculations for initially (a) edge and (b) screw oriented perfect dislocations in the pyramidal-II plane as determined by PFDD. Results for both pure Mg, and Ti are shown.

Table 6
Equilibrium stacking fault widths in units Å from the dissociation of edge and screw oriented perfect dislocations along the pyramidal-II plane in pure Mg reported previously in the literature and compared to values calculated with PFDD. The different methods are abbreviated as: phase field dislocation dynamics (PFDD), and density functional theory (DFT). In the PFDD calculations, the error bars correspond to $0.5d$, which is error due to the grid spacing used in the calculations.

Author	Edge (Å)	Screw (Å)	b (Å)	Method
This work	25.810 ± 0.679	19.018 ± 0.679	6.087	PFDD
	22.155	15.632		Analytical (Hirth and Lothe, 1968)
Ghazisaeidi et al. (2014)	18.3	16.6	6.106	DFT
Itakura et al. (2016)	–	14	6.0827	DFT
Kumar et al. (2017)	22.6	–	6.089	DFT

A few experimental observations as well as MD simulations have reported the perfect dislocations on the pyramidal-II slip plane to dissociate into two partials equal in magnitude and collinear according to (Kumar et al., 2017; Partridge, 1967; Rodney et al., 2017; Stohr and Poirier, 1972):

$$\frac{1}{3}\left[2\bar{1}\bar{1}3\right] \rightarrow \frac{1}{6}\left[2\bar{1}\bar{1}3\right] + \frac{1}{6}\left[2\bar{1}\bar{1}3\right]. \tag{24}$$

In the case of Mg, DFT has previously calculated the equilibrium SFW for both edge and screw dislocations on the pyramidal-II slip plane, as shown in Table 6. The equilibrium SFW as calculated with PFDD for both the edge and screw dislocation dissociation reactions are slightly higher, but compare well with those determined with DFT. We also note that there are further variations among the DFT results, possibly due to the use of different exchange correlation functionals and k-points, supercell sizes, initial dislocation configuration, and method of defining the SFW width. To the authors' knowledge, equilibrium SFW calculations have not been previously reported for edge or screw dislocation dissociations along the pyramidal-II plane in Ti.

Interestingly, the disregistry gradient $d\Delta/dx$ in Fig. 7 shows that the dissociated dislocations in Mg have an apparent asymmetry between the core widths of the two partials. The left partial has a much wider (~ 2.5 times wider) core than the right partial. Differences in the widths of the individual partials (partial core spreading) in the split pyramidal-II dislocation in Mg have also been reported in atomistic molecular dynamics calculations using the MEAM potential (Kumar et al., 2017; Wu et al., 2015). The distances these two partials glide during the dissociation are also unequal as well, with the left partial moving further to the left than the right partial. In the case of Ti, the partial core widths are not as dissimilar as in Mg, and the differences between the distances the right and left partial glide during the dissociation is less than that in Mg and favors glide of the right partial more than the left.

We surmise that the asymmetries in the Mg and Ti dislocation cores arise from the asymmetry of the positions and critical energetic values in their GSFE curves. First we consider the Burgers vectors of the two partials. The reaction in Eq. (24) suggests that the dissociation leads to two partials of equal Burgers vector. From the PFDD calculated core structure, we can determine the magnitude of the Burgers vector from the value of the disregistry Δ at $x = 0$. For Mg $\Delta(0)$ is ~ 0.5 and thus we can expect a dislocation split into partials with equal Burgers vectors, consistent with Eq. (24). For Ti, however, $\Delta(0)$ is ~ 0.45, meaning the left and right partials have a Burgers vector magnitude of $0.45b$ and $0.55b$ respectively, where b is the magnitude of the Burgers vector for the initial perfect dislocation. This asymmetry in the partial Burgers vector value is governed by the displacement needed to achieve the local minimum or intrinsic stacking fault energy I in the GSFE curve in Figs. 2(d) and 8. As shown in Fig. 7, unlike Mg, the Burgers vectors of the two dissociated pyramidal dislocations in Ti are not equal in magnitude.
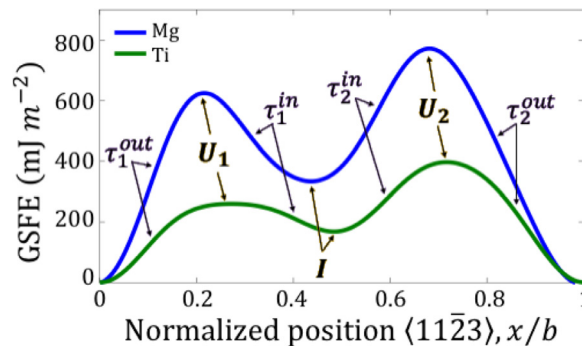

Fig. 8. GSFE curves for both Mg and Ti showing labels for critical energetic points and the peak shear stresses as the slopes leading to and from these points.

Table 7

The relationships between the absolute values for the maximum slopes between the global and local maxima and minima of the GSFE curves for the pyramidal-II planes of Mg and Ti as shown in Fig. 2(d).

Material	τ_1^{out}	τ_1^{in}	τ_2^{in}	τ_2^{out}	τ_1^{out}/τ_1^{in}	τ_2^{out}/τ_2^{in}	τ_2^{in}/τ_1^{in}	$\tau_2^{out}/\tau_1^{out}$
Mg	16.85	6.29	15.50	24.03	2.68	1.55	2.47	1.43
Ti	50.24	21.38	30.28	36.36	2.35	1.20	1.42	0.72

It is noticed that the partial with the wider core is associated with the lower unstable stacking fault peak U_1 (left) and the narrower one with the higher unstable stacking fault peak U_2 (right) in the GSFE curve (see Figs. 2(d) and 8). During the dissociation process, the lower peak barrier would pose less resistance to partial dislocation glide, permitting core spreading. For Ti, with the more symmetrical core structure the difference between the peak barriers in the Ti GSFE curve is comparatively smaller, apparently leading them to only a slight asymmetry between the core widths of the left and right partials.

Related to the peak energies U is the peak shear stress required to move the partial dislocations apart during the dissociation. These critical stresses are calculated directly from the derivative of the GSFE curves with respect to the displacement shift. The left partial would follow the energetic path starting from the reference point (global minimum at 0 shift) to U_1, whereas the right partial would follow a path associated with the right most reference point (global minimum at 1 to the peak U_2). The ideal shear stress associated with the resistance for the left partial to move is τ_1^{out} is the maximum slope from a global minimum to U_1, and that for the right partial is τ_2^{out}, the maximum slope from the global minimum to U_2. The local minimum in the GSFE corresponds to the stacking fault formed by the glide of the partials. The peak slopes on either side of the local minimum, τ_1^{in} and τ_2^{in}, are related to the resistance for the core of the partials to spread in plane. With interest in the effect of asymmetries in the GSFE with asymmetries in core structures, we analyze the ratios of these ideal shear stresses. Table 7 shows the four peak slopes and the ratios of $\tau_2^{out}/\tau_1^{out}$ and τ_2^{in}/τ_1^{in} as well as τ_1^{out}/τ_1^{in} and τ_2^{out}/τ_2^{in} for Mg and Ti.

According to Table 7, $\tau_2^{out}/\tau_1^{out}$ for Ti is less than unity, suggesting that it will be easier for the right partial to glide right than the left partial to glide left. As seen in the PFDD calculated core structure of the dissociated screw dislocation in Fig. 7(b), the left partial moves $\sim 0.9b$ left and the right partial moves $\sim 1.1b$ right. Conversely, for Mg $\tau_2^{out}/\tau_1^{out}$ is greater than unity, suggesting that it will be far easier for the left partial to glide left than the right partial to glide right. Accordingly, the core of the Mg pyramidal dislocations as calculated via PFDD finds that the left and right partials move $\sim 2.9b$ and $\sim 1.3b$, respectively for the dissociated edge dislocation and $\sim 2.0b$ and $\sim 1.1b$, respectively for the dissociated screw dislocation.

Once the SF has formed, whether or not the spreading of a partial dislocation core occurs is governed by τ_2^{in}/τ_1^{in}. Referring to Table 7, while τ_2^{in}/τ_1^{in} exceeds unity for both Ti and Mg, it is much higher in Mg than that for Ti, indicating that core spreading is more likely in one partial dislocation in Mg than Ti. Further, the ratios τ_1^{out}/τ_1^{in} and τ_2^{out}/τ_2^{in} indicate which partial dislocation is likely to experience this spreading. According to these values for Mg, we would anticipate spreading of the left partial core. In agreement, in simulation, the left partial in the pyramidal core of Mg is found to broadened widely, more so than the right one.

4. Summary

This work presents model extensions to advance a phase field approach for studying dislocation motion, called phase field dislocation dynamics (PFDD), to include crystals with a hexagonal close packed (HCP) crystal structure. The functional form of the lattice energy was modified to include periodic potentials that depend on slip mode. In this way, the significant differences seen in the γ-surfaces and GSFE curves on different HCP slip planes, as determined with atomistic approaches, can be represented. The new periodic potentials are directly informed by generalized stacking fault energy (GSFE) curves calculated with density functional theory (DFT), either calculated here or adopted from previously published DFT data. For instance, the γ-surface for the basal slip plane in Mg and the GSFE curve for the pyramidal-II slip plane in Ti are presented here.

With the model, we calculate the equilibrium SFWs for both edge and screw dislocations in various HCP metals, including pure Mg, $Mg_{47}Y$, Ti, and Zr, and on the basal, prismatic, and pyramidal-II slip planes. These examples illustrate the flexibility of the model formulation, as well as permit direct comparison with calculations of equilibrium SFW by other computational approaches, such as atomistic and other continuum approaches previously reported in the literature. For example, the method is able to capture both the compact dislocation core on the prismatic plane in Mg, and also the dissociated dislocation core on the prismatic plane in Zr and Ti. In all cases, the PFDD results show reasonable comparison to results previous reported using MD or DFT. Since PFDD was informed with DFT GSFE information, best comparisons are generally found with DFT calculated values, or GPN models also informed with DFT information. In addition, results were compared to analytical calculations of the equilibrium SFW (Hirth and Lothe, 1968). In all cases, the analytical values were larger than those determined by PFDD. The analytical equation does not fully account for the dissociation process, including energy barriers partials must overcome as they spread apart through the crystal lattice. In addition, it is worth noting that in some

cases, such as screw and edge dislocations in Zr and Ti on the pyramidal-II plane, data for the equilibrium core structures were not available in the current literature for comparison.

In simulating the dissociation process from an initially unstable perfect dislocation to its final equilibrium structure, the PFDD model revealed additional effects of the displacements and values of energetic local maxima and minima of the GSFE curve. The most pronounced example arose when considering the structure of dislocations on the pyramidal-II plane, which has an asymmetrical GSFE curve. In the case of Mg, the PFDD results show that the width of the left partial is nearly three times wider than the right partial, for a dissociated edge dislocation. It is also shown that while the Burgers vectors for the partial dislocations are equal in magnitude, the left partial glides farther than the right partial. Consequently, the left partial contributes more to the total SFW than the right partial. These results are in agreement with previous work using atomistic calculations with the MEAM potential, which also found an asymmetry in the width of individual partials along the pyramidal-II plane in Mg (Kumar et al., 2017; Wu et al., 2015). With the aid of PFDD calculations with designed GSFE curves, we identify the relationships between the asymmetries in the GSFE curve and the asymmetries in the equilibrium core structure of the dislocation, namely distances traveled by the two partials as they glide apart during the dissociation and in the core widths and values of the Burgers vectors of the two partial dislocations, explaining why the extended dislocation structures exhibit significant differences in asymmetry between Mg and Ti. On the other hand, while Ti also has a GSFE curve that possesses some asymmetries, its pyramidal dislocation core structure bears less asymmetric characteristics than the Mg pyramidal dislocation core. Our analysis reveals that the partials in Ti have Burgers vectors with different magnitudes that correspond to the position of the intrinsic stacking fault energy, such that the left partial has a smaller Burgers vector than the right partial.

We mention that other dislocations have been reported in HCP materials. In both Zr and Ti, another important pyramidal slip system is pyramidal type I, which has twelve slip systems. For Mg, whether this system is as active or more active than the pyramidal type II mode studied here has been a point of debate. This is a potential area for future work with the newly extended HCP-PFDD model.

HCP metals, particularly in pure form, as studied here, tend to twin easily when the c-axis of the crystals are stretched or compressed. The role of dislocations in the formation of deformation twin nuclei has been studied predominantly using dislocation theory and atomistic simulation (Beyerlein and Wang, 2019; Wang and Beyerlein, 2012a; Wang et al., 2013; 2014b). It has been suggested that twin embryo formation begins with the stress-induced dissociation of linear defects with relatively large Burgers vectors, such a pyramidal dislocation or pile up of basal dislocations (Beyerlein et al., 2012; Capolungo and Beyerlein, 2010; Mendelson, 1970). While in this study we do not simulate twin formation, we simulate the dissociation process of individual dislocations. These calculations would be fundamental to further calculations of dislocation reactions among many dislocations with the PFDD model presented here.

Declaration of Competing Interest

None.

CRediT authorship contribution statement

C. Albrecht: Conceptualization, Software, Validation, Investigation, Data curation, Formal analysis, Funding acquisition, Visualization. **A. Hunter:** Software, Methodology. **A. Kumar:** Data curation. **I.J. Beyerlein:** Supervision, Project administration, Funding acquisition, Resources.

Acknowledgements

References

Ardeljan, M., Knezevic, M., Jain, M., Pathak, S., Kumar, A., Li, N., Mara, N.A., Baldwin, J.K., Beyerlein, I.J., 2018. Room temperature deformation mechanism of Mg/Nb nanolayered composites. J. Mater. Res. 33 (10), 1311–1332.
Ardeljan, M., Savage, D.J., Kumar, A., Beyerlein, I.J., Knezevic, M., 2016. The plasticity of highly oriented nano-layered Zr/Nb composites. Acta Mater. 115, 189–203.
Bertin, N., Tomé, C.N., Beyerlein, I.J., Barnett, M.R., Capolungo, L., 2014. On the strength of dislocation interactions and their effect on latent hardening in pure magnesium. Int. J. Plast. 62, 72–92.
Beyerlein, I.J., Hunter, A., 2016. Understanding dislocation mechanics at the mesoscale using phase field dislocation dynamics. Philos. Trans. R. Soc. A 374, 20150166.
Beyerlein, I.J., Wang, J., 2019. Interface-driven mechanisms in cubic/noncubic nanolaminates at different scales. MRS Bull. 44, 31–39.
Beyerlein, I.J., Wang, J., Barnett, M.R., Tomé, C.N., 2012. Double twinning mechanisms in magnesium alloys via dissociation of lattice dislocations. Proc. R. Soc. A 468, 1496–1520.

Cahn, J.W., Hilliard, J.E., 1958. Free energy as a non-uniform system. I. Interfacial energy. J. Chem. Phys. 28, 258–267.

Cao, L., Hunter, A., Beyerlein, I.J., Koslowski, M., 2015. The role of partial mediated slip during quasi-static deformation of 3D nanocrystalline metals. J. Mech. Phys. Solids 78, 415–426.

Capolungo, L., Beyerlein, I.J., 2010. Nucleation and stability of twins in hcp metals. Phys. Rev. B 78, 024117.

Capolungo, L., Beyerlein, I.J., Wang, Z.Q., 2010. The role of elastic anisotropy on plasticity in hcp metals: a three-dimensional dislocation dynamics study. Modell. Simul. Mater. Sci. Eng. 18, 085002.

Clouet, E., 2012. Screw dislocation in zirconium: an ab initio study. Phys. Rev. B 86, 144104.

Clouet, E., Caillard, D., Chaari, N., Onimus, F., Rodney, D., 2015. Dislocation locking versus easy glide in titanium and zirconium. Nat. Mater. 14, 931–936.

Daw, M.S., Baskes, M.I., 1984. Embedded-atom method: derivation and application to impurities, surfaces, and other defects in metals. Phys. Rev. B 29 (12), 6443–6453.

Domain, C., 2006. Ab initio modelling of defect properties with substitutional and interstitials elements in steels and Zr alloys. J. Nucl. Mater. 351, 1–19.

Domain, C., Besson, A., 2004. Atomic-scale ab initio study of the Zr–H system: ii. Interaction of H with plane defects and mechanical properties. Acta Mater. 52, 1495–1502.

Fan, T.W., Zhang, Q., Ma, L., Tang, P.Y., Tang, B.Y., Peng, L.M., Ding, W.J., 2014. First-principles study of the dislocation core structures on basal plane in magnesium. Eur. J. Mech. A/Solids 45, 1–7.

Farenc, S., Caillard, D., Couret, A., 1993. An in situ study of prismatic glide in titanium at low temperatures. Acta Metall. Mater. 41 (9), 2701–2709.

Farenc, S., Caillard, D., Couret, A., 1995. A new model for the peak of activation area of titanium. Acta Metall. Mater. 43 (10), 3669–3678.

Ghazisaeidi, M., Hector, L.G., Curtin, W.A., 2014. First-principles core structures of $< c + a >$ edge and screw dislocations in Mg. Scr. Mater. 75, 42–45.

Groh, S., Marin, E.B., Horstemeyer, M.F., Bammann, D.J., 2009. Dislocation motion in magnesium: a study by molecular statics and molecular dynamics. Modell. Simul. Mater. Sci. Eng. 17 (7).

Hill, R., 1952. The elastic behavior of a crystalline aggregate. Proc. Phys. Soc. Sect. A 65, 349–354.

Hirth, J.P., Lothe, J., 1968. Theory of Dislocations. McGraw-Hill, New York.

Hunter, A., Beyerlein, I.J., 2013. Unprecedented grain size effect on stacking fault width. Appl. Phys. Lett. Mater. 1 (032109), 1–9.

Hunter, A., Beyerlein, I.J., 2014. Predictions of an alternative pathway for grain-boundary driven twinning. Appl. Phys. Lett. 104 (233112), 1–4.

Hunter, A., Beyerlein, I.J., 2015. Relationship between monolayer stacking faults and twins in nanocrystals. Acta Mater. 88, 207–217.

Hunter, A., Beyerlein, I.J., Germann, T.C., Koslowski, M., 2011. Influence of the stacking fault energy surface on partial dislocations in FCC metals with a three-dimensional phase field model. Phys. Rev. B 84 (144108), 1–10.

Hunter, A., Leu, B., Beyerlein, I.J., 2018. A review of slip transfer: applications of mesoscale techniques. J. Mater. Sci. 53, 5584–5603.

Hunter, A., Zhang, R.F., Beyerlein, I.J., 2014. The core structure of dislocation and their relationship to the material γ-surface. J. Appl. Phys. 115, 134314.

Itakura, M., Kaburaki, H., Yamaguchi, M., Tsuru, T., 2016. Novel cross-slip mechanism of pyramidal screw dislocations in magnesium. Phys. Rev. Lett. 116, 225501.

Kaxiras, E., Duesbery, M.S., 1993. Free energies of generalized stacking faults in Si and implications for the brittle-ductile transition. Phys. Rev. Lett. 70 (24), 3752–3755.

Koslowski, M., Cuitiño, A., Ortiz, M., 2002. A phase-field theory of dislocations dynamics, strain hardening and hysteresis in ductile single crystals. J. Mech. Phys. Solids 50 (12), 2597–2635.

Kresse, G., Furthmüller, J., 1996. Efficiency of ab initio total energy calculations for metals and semiconductors using a plane-wave basis set. Comput. Mater. Sci. 6 (1), 15–50.

Kresse, G., Furthmüller, J., 1996. Efficient iterative schemes for ab initio total-energy calculations using a plane-wave basis set. Phys. Rev. B 54 (16), 11169–11186.

Kumar, A., Morrow, B., McCabe, R.J., Beyerlein, I.J., 2017. An atomic-scale modeling and experimental study of $< c + a >$ dislocations in Mg. Mater. Sci. Eng. A 695, 270–278.

Lei, L., Marian, J.L., Koslowski, M., 2013. Phase-field modeling of defect nucleation and propagation in domains with material inhomogeneities. Modell. Simul. Mater. Sci. Eng. 21 (025009), 1–15.

Louchez, M.A., Thuinet, L., Besson, R., Legris, A., 2017. Microscopic phase-field modeling of hcp|fcc interfaces. Comput. Mater. Sci. 132, 62–73.

Lu, G., Kioussis, N., Bulatov, V.V., Kaxiras, E., 2000. Generalized-stacking-fault energy surface and dislocation properties of aluminum. Phys. Rev. B 62 (5), 3099–3108.

MATLAB and Curve Fitting Toolbox Release, 2016b. The MathWorks, Inc.. Natick, Massachusetts, United States.

Mendelson, S., 1970. Dislocation dissociations in hcp metals. J. Appl. Phys. 41 (1893).

Mianroodi, J.R., Hunter, A., Beyerlein, I.J., Svendsen, B., 2016. Theoretical and computational comparison of models for dislocation dissociation and stacking fault/core formation in fcc systems. J Mech Phys Solids 95, 719–741.

Mianroodi, J.R., Svendsen, B., 2015. Atomistically determined phase-field modeling of dislocation dissociation, stacking fault formation, dislocation slip, and reactions in fcc systems. J. Mech. Phys. Solids 77, 109–122.

Naka, S., Lasalmonie, A., Costa, P., Kubin, L., 1988. The low-temperature plastic deformation of titanium and the core structure of a-type screw dislocations. Philos. Mag. A 57 (5), 717–740.

Partridge, P.G., 1967. The crystallography and deformation modes of hexagonal close-packed metals. Metall. Rev. 12 (1), 169–194.

Pei, Z., Zhu, L.-F., Friak, M., Snadlobes, S., von Pezold, J., Sheng, H., Race, C., Zaefferer, S., Svendsen, B., Raabe, D., Neugebauer, J., 2013. Ab initio and atomistic study of generalized stacking fault energies in Mg and Mg-Y alloys. New J. Phys. 15, 043020.

Peng, X., Mathew, N., Beyerlein, I.J., Dayal, K., Hunter, A., 2020. A 3D phase field dislocation dynamics model for body-centered cubic crystals. Comput. Mater. Sci. 171, 109217.

Perdew, J.P., Burke, K., Ernzerhof, M., 1996. Generalized gradient approximation made simple. Phys. Rev. Lett. 77 (18), 3865–3868.

Pi, Z.P., Fang, Q.H., Jiang, C., Liu, B., Liu, Y., Wen, P.H., Liu, Y.W., 2017. Stress dependence of the dislocation core structure and loop nucleation for face-centered-cubic metals. Acta Mater. 131, 380–390.

Qiu, D., Zhao, P., Shen, C., Lu, W., Zhang, D., Mrovec, M., Wang, Y., 2019. Predicting grain boundary structure and energy in BCC metals by integrated atomistic and phase-field modeling. Acta Mater. 164, 799–809.

Rodney, D., Ventelon, L., Clouet, E., Pizzagalli, L., Willaime, F., 2017. Ab initio modeling of dislocation core properties in metals and semiconductors. Acta Mater. 124, 633–659.

Schoeck, G., 2001. The core structure, recombination energy and Peierls energy for dislocations in al. Philos. Mag. A 81 (5), 1161–1176.

Schoeck, G., 2005. The Peierls model: progress and limitations. Mater. Sci. Eng. A 400–401, 7–17.

Shang, S.L., Wang, W.Y., Zhou, B.C., Wang, Y., Darling, K.A., Kecskes, L.J., Mathaudhu, S.N., Liu, Z.K., 2014. Generalized stacking fault energy, ideal strength and twinnability of dilute Mg-based alloys: a first-principles study of shear deformation. Acta Mater. 67, 168–180.

Shen, C., Wang, Y., 2003. Phase field model of dislocation networks. Acta Mater. 51, 2595–2610.

Shen, C., Wang, Y., 2004. Incorporation of γ-surface to phase field model of dislocation: simulating dislocation dissociation in fcc crystals. Acta Mater. 52, 683–691.

Shen, L., Proust, G., Ranzi, G., 2014. An atomistic study of dislocation-solute interaction in Mg-Al alloys. In: IOP Conference Series: Materials Science and Engineering, 10.

Steinbach, I., 2009. Phase-field models in materials science. Modell. Simul. Mater. Sci. Eng. 17, 073001.

Stohr, J.F., Poirier, J.P., 1972. Etude en microscopie electronique du glissement pyramidal dans le magnesium. Philos. Mag. 25 (6), 1313–1329.

Svendsen, B., Shanthraj, P., Raabe, D., 2018. Finite-deformation phase-field chemomechanics for multiphase, multicomponent solids. J. Mech. Phys. Solids 112, 619–636.

Udagawa, Y., Yamaguchi, M., Tsuru, T., Abe, H., Sekimura, N., 2010. Effect of Sn and Nb on generalized stacking fault energy surfaces in zirconium and gamma hydride habit planes. Philos. Mag. 58, 3927–3938.

Vitek, V., 1968. Intrinsic stacking faults in body-centered cubic crystals. Philos. Mag. 18 (154), 773–786.

Wang, J., Beyerlein, I.J., 2012. Atomic structures of [1011] symmetric tilt grain boundaries in hexagonal close packed (hcp) crystals. Metall. Mater. Trans. A 43, 3556–3569.

Wang, J., Beyerlein, I.J., 2012. Atomic structures of symmetric tilt grain boundaries in hexagonal close packed (hcp) crystals. Modell. Simul. Mater. Sci. Eng. 20, 024002.

Wang, J., Beyerlein, I.J., Hirth, J.P., 2012. Nucleation of elementary {1̄011} and {1̄013} twinning dislocations at a twin boundary in hexagonal close-packed crystals. Modell. Simul. Mater. Sci. Eng. 20, 024001.

Wang, J., Beyerlein, I.J., Tomé, C.N., 2014. Reactions of lattice dislocations with grain boundaries in Mg: implications on the micro scale from atomic-scale. Int. J. Plast. 56, 156–172.

Wang, J., Yadav, S.K., Hirth, C.N., Tomé, C.N., Beyerlein, I.J., 2013. Pure-shuffle nucleation of deformation twins in hexagonal-close-packed metals. Mater. Res. Lett. 1, 126–132.

Wang, J., Yu, Q., Jiang, Y., Beyerlein, I.J., 2014. Twinning-associated boundaries in hexagonal close-packed metals. J. Miner. Metals Mater.Soc. 66, 95–101.

Wang, R., Wang, S.F., Wu, X.Z., Wei, Q.Y., 2010. First-principles determination of dislocation properties in magnesium based on the improved Peierls-Nabarro equation. Phys. Scr. 81 (6).

Wang, Y., Li, J., 2010. Phase field modeling of defects and deformation. Acta Mater. 58, 1212–1235.

Wang, Y.U., Jin, Y.M., Cuitiño, A.M., Khachaturyan, A.G., 2001. Nanoscale phase field microelasticity theory of dislocations: model and 3D simulations. Acta Mater. 49, 1847–1857.

Wu, Z., Francis, M.F., Curtin, W.A., 2015. Magnesium interatomic potential for simulating plasticity and fracture phenomena. Modell. Simul. Mater. Sci. Eng. 23 (1), 1–19.

Xu, S., Mianroodi, J.R., Hunter, A., Beyerlein, I.J., Svendsen, B., 2019. Phase-field-based calculations of the disregistry fields of static extended dislocations in fcc metals. Philos. Mag. 99 (11), 1400–1428.

Yasi, J.A., Nogaret, T., Trinkle, D.R., Qi, Y., Hector, G., Curtin, W.A., 2009. Basal and prism dislocation cores in magnesium: comparison of first-principles and embedded-atom-potential methods predictions. Modell. Simul. Mater. Sci. Eng. 17 (5).

Yin, B., Wu, Z., Curtin, W.A., 2017. Comprehensive first-principles study of stable stacking faults in hcp metals. Acta Mater. 123, 223–234.

Yoo, M., 1969. Interaction of slip dislocations with twins in hcp metals. Trans. Metall. Soc. AIME 245, 2051–2060.

Zeng, Y., Hunter, A., Beyerlein, I.J., Koslowski, M., 2016. A phase field dislocation dynamics model for a bicrystal interface system: an investigation into dislocation slip transmission across cube-on-cube interfaces. Int. J. Plast. 79, 293–313.

Zhao, P., Shen, C., Savage, M.F., Li, J., Niezgoda, S.R., Mills, M.J., Wang, Y., 2019. Slip transmission assisted by Shockley partials across α/β interfaces in Ti-alloys. Acta Mater. 171, 291–305.